Controlling the helicity of light by electrical magnetization switching

https://doi.org/10.1038/s41586-024-07125-5

Received: 15 September 2023

Accepted: 26 January 2024

Published online: 27 March 2024

Check for updates

Pambiang Abel Dainone[1], Nicholas Figueiredo Prestes[2], Pierre Renucci[3], Alexandre Bouché[1], Martina Morassi[4], Xavier Devaux[1], Markus Lindemann[5], Jean-Marie George[2], Henri Jaffrès[2], Aristide Lemaitre[4], Bo Xu[6,7], Mathieu Stoffel[1], Tongxin Chen[1], Laurent Lombez[3], Delphine Lagarde[3], Guangwei Cong[8], Tianyi Ma[9], Philippe Pigeat[1], Michel Vergnat[1], Hervé Rinnert[1], Xavier Marie[3], Xiufeng Han[9], Stephane Mangin[1], Juan-Carlos Rojas-Sánchez[1], Jian-Ping Wang[10], Matthew C. Beard[11], Nils C. Gerhardt[5], Igor Žutić[12] & Yuan Lu[1]✉

Controlling the intensity of emitted light and charge current is the basis of transferring and processing information[1]. By contrast, robust information storage and magnetic random-access memories are implemented using the spin of the carrier and the associated magnetization in ferromagnets[2]. The missing link between the respective disciplines of photonics, electronics and spintronics is to modulate the circular polarization of the emitted light, rather than its intensity, by electrically controlled magnetization. Here we demonstrate that this missing link is established at room temperature and zero applied magnetic field in light-emitting diodes[2–7], through the transfer of angular momentum between photons, electrons and ferromagnets. With spin–orbit torque[8–11], a charge current generates also a spin current to electrically switch the magnetization. This switching determines the spin orientation of injected carriers into semiconductors, in which the transfer of angular momentum from the electron spin to photon controls the circular polarization of the emitted light[2]. The spin–photon conversion with the nonvolatile control of magnetization opens paths to seamlessly integrate information transfer, processing and storage. Our results provide substantial advances towards electrically controlled ultrafast modulation of circular polarization and spin injection with magnetization dynamics for the next-generation information and communication technology[12], including space–light data transfer. The same operating principle in scaled-down structures or using two-dimensional materials will enable transformative opportunities for quantum information processing with spin-controlled single-photon sources, as well as for implementing spin-dependent time-resolved spectroscopies.

The rapid growth of information and communication technology results in increasing power consumption dominated by transferring rather than processing information[13]. This is demonstrated by the global internet traffic that increased by 40% between February and mid-April 2020 during the COVID-19 containment[14], whereas data centres alone are predicted to require 8% of globally generated electrical power by 2030 (ref. 15). To overcome this situation and the related von Neumann bottleneck[16], there is a push to develop integrated multifunctional single-chip platforms that combine magnetic storage, optical transmission and CMOS processing, while recognizing the importance of energy-efficient optical communication with enhanced bandwidth[17]. A promising direction is to use the left/right circularly polarized light or photons with negative/positive helicity, because their spin angular momentum can be directly coupled to the spin of electrons, with applications from quantum information processing[18] and three-dimensional displays[19] to optical sensors[20] and encryption[21]. In spintronics, this light–matter interaction provides an effective source of spin information and overcomes the limitation of carrier spin imbalance in solids to typical lengths (less than μm) and timescales (less than ns). Instead, from the conservation of total angular momentum, the information of spin imbalance of carriers (spin polarization) can be transferred much farther and faster through the circular polarization of the emitted light with polarization degree[3] $P_c = (S^{\sigma+} - S^{\sigma-})/(S^{\sigma+} + S^{\sigma-})$, where $S^{\sigma+}$ is the right circularly polarized photon density and $S^{\sigma-}$ is the left circularly polarized photon density.

[1]Institut Jean Lamour, Université de Lorraine, CNRS, UMR 7198, Nancy, France. [2]Laboratoire Albert Fert, CNRS, Thales, Université Paris-Saclay, Palaiseau, France. [3]Université de Toulouse, INSA-CNRS-UPS, LPCNO, Toulouse, France. [4]Université Paris-Saclay, CNRS, Centre de Nanosciences et de Nanotechnologies, Palaiseau, France. [5]Photonics and Terahertz Technology, Ruhr-Universität Bochum, Bochum, Germany. [6]Key Laboratory of Semiconductor Materials Science, Institute of Semiconductors, Chinese Academy of Sciences, Beijing, China. [7]College of Materials Science and Opto-Electronic Technology, University of Chinese Academy of Sciences, Beijing, China. [8]Platform Photonics Research Center, National Institute of Advanced Industrial Science and Technology, Tsukuba, Japan. [9]Beijing National Laboratory for Condensed Matter Physics, Institute of Physics, University of Chinese Academy of Sciences, Chinese Academy of Sciences, Beijing, China. [10]Department of Electrical and Computer Engineering, University of Minnesota, Minneapolis, MN, USA. [11]Chemistry and Nanoscience Center, National Renewable Energy Laboratory, Golden, CO, USA. [12]Department of Physics, University at Buffalo, State University of New York, Buffalo, NY, USA. ✉e-mail: yuan.lu@univ-lorraine.fr

In spin-lasers with optically injected spin-polarized carriers, ultrafast P_c switching at above 200 GHz is about one order of magnitude faster than the fastest intensity-modulated lasers and simultaneously supports an ultralow power operation[12]. Although this advance is encouraging for the P_c-encoded information transfer, the optically generating spin-polarized carrier is impractical for many applications. The key challenge is modulating P_c through electrically controlled magnetization, which would combine electron and photon spin with the nonvolatile properties of ferromagnets, to integrate transferring, processing and storing information effectively[22]. The importance of this breakthrough is well recognized. Even without integrating magnetization dynamics, changing electrically controlled P_c in atomically thin semiconductors, WSe_2, by combining the effects of anisotropic band structure and applied electric field in electric-double-layer transistor[23] or light-emitting diode (LED)[24] has attracted considerable interest. In both cases, modulating P_c is not decoupled from modulating the light intensity that limits the P_c-encoded information transfer. By integrating GaAs semiconductor-based LEDs with a pair of ferromagnets having antiparallel magnetizations, M, P_c can be modulated by varying the current injected into each of the ferromagnets to inject carriers of opposite spins, thus contributing to the emission of opposite helicity[25]. Such a spin-LED is attractive because its operation is directly coupled to the nonvolatile M. However, switching P_c in this manner is complicated because it requires alternating currents injected into the different ferromagnets, thus removing the advantage compared with the conventional intensity modulation. Extending this design principle to spin-lasers[26,27], which are necessary for ultrafast operation and can be viewed as LEDs with resonant cavities adding optical gain, possesses inherent disadvantages (Supplementary Note 1). A large separation (several microns) from the ferromagnet to the active region of the laser, in which the electrons and holes recombine, exceeds the spin-diffusion length and substantially diminishes the degree of carrier spin polarization that determines the P_c amplitude change[28].

Device design

In this work, we use an innovative approach to establish the missing link between photonics, electronics and spintronics. A single ferromagnet injects electron spins in an LED, whereas a commercially established spin–orbit torque (SOT) electrically switches M, which in turn controls the changes in P_c at room temperature and zero applied magnetic field. Despite the apparent simplicity of this approach with common materials, in Supplementary Note 2 we document the development obstacles for the SOT spin injector and identify subtle material challenges to be overcome. Figure 1a describes the principle of M switching. Passing a steady-state or pulsed charge current, I, in the spin injector channel, consisting of a ferromagnet–heavy metal junction, is accompanied by a spin Hall effect (SHE) in the heavy metal with strong spin–orbit coupling, in which the electrons with opposite spins (**s**) are pushed in the opposite directions perpendicular to I. The misalignment of these spins with an out-of-plane M of the ferromagnet leads to its twisting or SOT. The SOT-related damping-like torque, $\tau_{SO} \propto \mathbf{M} \times (\mathbf{M} \times \mathbf{s})$, generates a spin–orbit field, H_{SO} (ref. 29), to switch the out-of-plane M if I is large enough. With a small applied constant in-plane field, H_{ext}, M can be deterministically switched even with alternating the direction of I and its pulsed behaviour. Ultimately, very short current pulses (a few ps)[30] would enable an ultrafast operation, whereas using textured ferromagnetic layers[31], in-plane exchange bias[32] or a substrate with suitable crystalline orientations[33] removes the need for any H_{ext}. The top view of an integrated SOT spin-LED device is shown in Fig. 1b. A pulsed current, I_{pulse}, is injected in the lateral direction to switch M, whereas a vertical bias, V_{bias}, is applied to emit the light, with P_c determined by the direction of the injected spin. Our quantum-dot-based spin-LED in Fig. 1c shows that the spin injector is less than 100 nm away from the active quantum-dot region in which the electron–hole recombination leads to the light emission. Although LEDs are already important building blocks for integrated photonics[34], this design is also compatible with future spin-lasers, in which the proximity of the spin injector to the active region ensures large P_c modulation. A high-resolution scanning transmission electron microscopy (HR-STEM) image in Fig. 1d shows that the spin injector includes common materials, such as tunnel barrier: MgO, ferromagnet: CoFeB, and heavy metal: Ta, which are used for commercial spintronic applications in magnetically storing information[29]. An important innovation is adding a 3-nm thick Cr in the injector that yields several advantages: (1) It largely reduces the channel resistance to 300 Ω, which strongly increases the breakdown current of the Schottky barrier to overcome the semiconductor shunting problem (Supplementary Note 2). (2) Cr produces a large spin Hall angle, θ_{SH}. With tunnelling spin Hall spectroscopy, we have measured a large θ_{SH} about −0.1 for Cr (ref. 35). As the sign of θ_{SH} for Cr and Ta is the same, this could enhance the SOT for M switching. (3) Cr can produce a large orbital current using the orbital Hall effect with an opposite sign compared with its spin Hall angle[36,37]. However, through a negative orbital-to-spin current conversion process by the inserted 3-nm thick Ta (spin–orbit correlation factor of Ta $\eta_{L\text{-}S} < 0$; ref. 38), Cr could also enhance SOT for M switching. Detailed information about the sample preparation and materials characterization is given in the Methods.

Magnetization switching of the injector

To study M switching, we use the anomalous Hall effect (AHE)[2,29], which, for a finite out-of-plane M, leads to the spin imbalance and the resulting voltage in the direction transverse to I (V_{AHE} between the contacts 3 and 4 in Fig. 1a). The corresponding AHE resistance[2], $R_{AHE} \sim M$, and its reversal indicates the out-of-plane M switching, measured in Fig. 2a as a function of out-of-plane field H_z and in Fig. 2b as a function of I_{pulse} with the duration, t_{pulse} = 0.1 s, at a fixed small in-plane field H_x = −10 mT. A constant channel current of 1 mA is applied to measure R_{AHE}. Grown on an LED substrate, the spin injector shows a robust M switching, from 140 K to 300 K, with varying either H_z or I_{pulse}. Square-like hysteresis loops in Fig. 2a confirm a good perpendicular magnetic anisotropy (PMA) of the injector. From Fig. 2b at 300 K, the critical switching current density is about 9.6×10^6 A cm^{-2}, comparable with the values reported for MgO/CoFeB/Ta system[10,39]. On reversal of the in-plane H_x, the polarity of the current-induced switching loop also reverses, which is consistent with the SOT-driven M switching (Extended Data Fig. 2). The full M switching cannot be realized without in-plane field (H_x = 0 T) (Fig. 2c), which is important to break the SOT symmetry for deterministic perpendicular switching[40]. From the change of R_{AHE} compared with that measured in Fig. 2a, we can estimate that 52% of magnetic domains have been switched at H_x = 0 T.

We use magneto-optic Kerr effect (MOKE) microscope images (Fig. 2d,e) to study the magnetic domain propagation with different t_{pulse} and I_{pulse}. At room temperature, with t_{pulse} = 0.1 s, a single I_{pulse} = 20 mA is large enough to fully switch M with a small in-plane field. However, when reducing t_{pulse} to 1 ms (Fig. 2d), a larger I_{pulse} up to 55 mA is needed to achieve single pulse switching. With smaller I_{pulse} = 45 mA, M is gradually switched with increasing pulse number (Fig. 2e). With 10 pulses, M can be completely switched. In our system, t_{pulse} for M switching is much longer than that reported for the CoFeB/MgO/Ta system[41]. This could be because of the strong pinning sites in the injector channel preventing the domain wall propagation in the creep regime[42] and related to the Ta diffusion inside CoFeB or structure defects for CoFeB/MgO on GaAs substrate (Extended Data Fig. 1). However, this pulse duration is not a fundamental obstacle. In a different sample with a W-based spin injector (Supplementary Note 4), we can reduce t_{pulse} to at least 10 μs, whereas the actual value might be even lower and is limited by our measurement technique. With future improvements in injector structure and channel geometry, a shorter t_{pulse} can be expected.

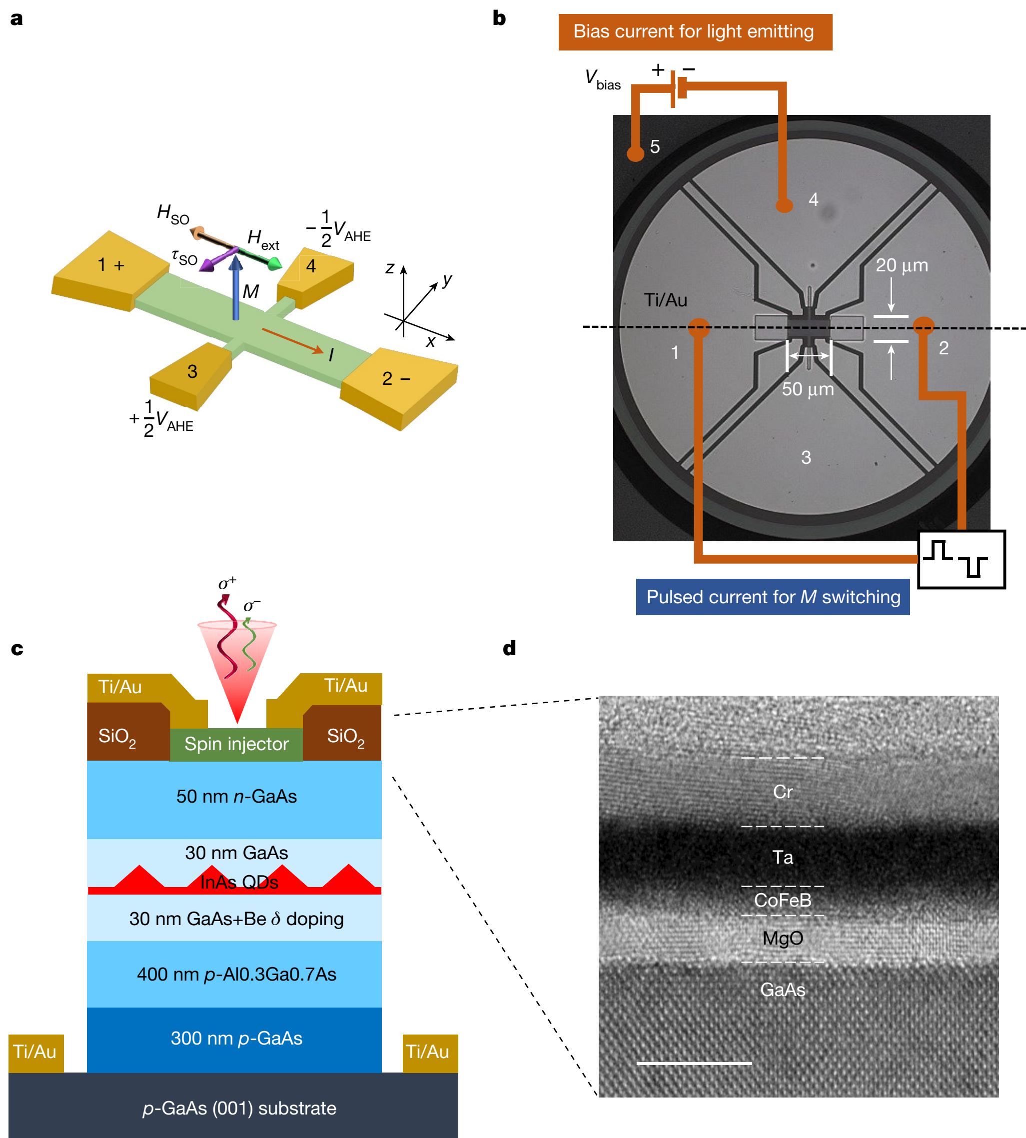

Fig. 1 | Structure of SOT spin-LED. **a**, Schematic of the magnetization switching in the injector Hall bar structure by the SHE. To monitor M switching, the anomalous Hall resistance, R_{AHE}, is measured by probing the Hall voltage, V_{AHE}, between contacts 3 and 4 in the direction transverse to I (injected between contacts 1 and 2). **b**, Top view of the optical microscopy image of the SOT spin-LED device. A pulsed current, I_{pulse}, is injected in the spin injector channel (between electrodes 1 and 2) to switch the magnetization, while a vertical bias, V_{bias}, is applied to pump the LED (between electrodes 4 and 5). **c**, Schematic side view of the spin-LED structure with an InAs quantum dot active layer. The spin injector consists of MgO(2.5 nm)/CoFeB(1.2 nm)/Ta(3 nm)/Cr(3 nm). **d**, Enlarged HR-STEM bright-field image showing the injector multilayer structure. Scale bar, 5 nm (**d**).

Electrical control of polarization

We next compare V_{bias}-dependent polarization-resolved electroluminescence for standard and SOT spin-LEDs to characterize P_c (H_z, T, V_{bias}) (Methods). In Fig. 3a, both spin-LEDs validate our highly efficient spin injector at room temperature and zero applied field. For the SOT spin-LED, P_c decreases from 30% at V_{bias} = 1.7 V to 18% at 3.1 V. Detailed V_{bias}-dependent polarization-resolved electroluminescence spectra are shown in Extended Data Fig. 4. The standard spin-LED with a large circular injector shows nearly constant P_c ~ 36%, even up to V_{bias} = 4.5 V. This difference can be explained by an approximately 60 times smaller injector area in the SOT spin-LED. As the product of the metal–insulator–semiconductor (MIS) junction resistance and the injector area $R \cdot A \propto e^d$, where d is MgO thickness, is constant, the smaller injector area yields a larger junction resistance R. Therefore, the voltage drop across the MgO barrier becomes more significant in the SOT spin-LED because the total voltage is applied across a series resistor consisting of a MIS junction and a semiconductor n-i-p junction. This results in a higher kinetic energy, E_k, of injected electrons (Fig. 3a, inset) than in the standard spin-LED. As the spin-flip rate is $\propto E_k^3$ in the Dyakonov–Perel spin-relaxation mechanism[2], P_c decreases more rapidly in the SOT spin-LED at large V_{bias} (refs. 4,43).

To verify the P_c control by M switching, we first used a single I_{pulse} = 30 mA with t_{pulse} = 0.1 s and then measured P_c, shown in Fig. 3b for V_{bias} = 1.9 V after M switching with positive and negative I_{pulse}. During the SOT switching, a small H_x = +10 mT was applied, whereas P_c was measured at H_x = 0 T and H_z = 0 T. These results show that the intensities of σ+ and σ− luminescence have been modulated depending on the pulsed-current direction. As a consequence, the P_c can be switched from +31% to −31%. As shown in Fig. 3c, the control of P_c remains possible even at zero field. A partial 52% M switching (Fig. 2c) explains why the modulation amplitude of P_c becomes smaller (around ±12%). However, as a stable two-state switching can still be fulfilled at H_x = 0 T, these results are very encouraging for future practical applications.

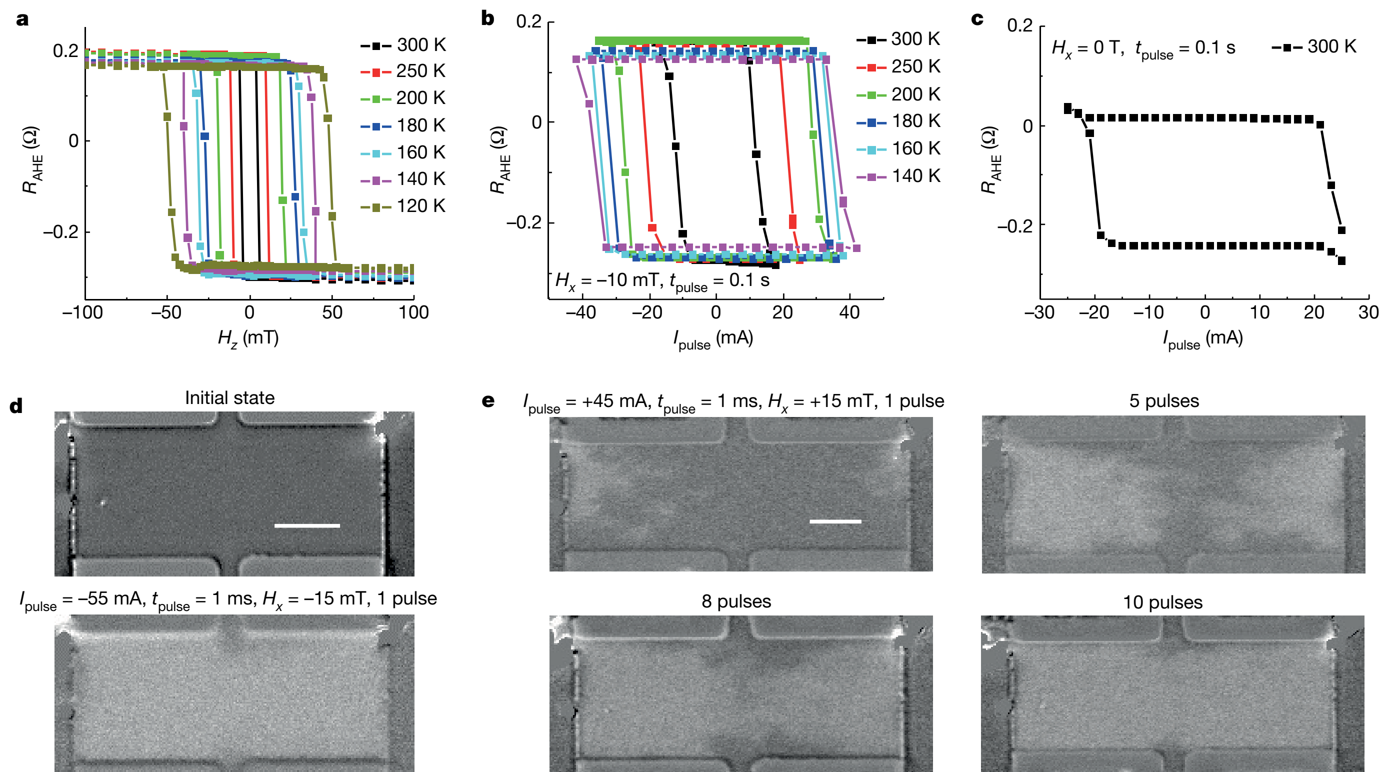

Fig. 2 | SOT switching injector magnetization. a, R_{AHE} of the spin injector on top of the LED structure as a function of the out-of-plane magnetic field at different temperatures. **b**, R_{AHE} of the spin injector as a function of the pulsed current at different temperatures with a small in-plane field of H_x = −10 mT for switching. **c**, R_{AHE} of the spin injector as a function of pulsed current injected in the injector channel with zero in-plane field for switching at 300 K. **d**, Room temperature (RT) MOKE images of the injector Hall bar channel after applying one single pulse of −55 mA (t_{puls} = 1 ms) with H_x = −15 mT. **e**, Room temperature MOKE images of the injector Hall bar channel after applying different numbers of pulses of +45 mA (t_{pulse} = 1 ms) with H_x = +15 mT. Error bars are smaller than data points in **a**–**c**. Scale bar, 10 µm (**d**,**e**).

Furthermore, for spin-lasers, a few per cent spin polarization of injected carriers can already result in P_c ~ 100% (refs. 44,45).

To verify the stability of P_c for repeated switching, we consider switching for 30 cycles. For each cycle, I_{pulse} = +25 mA and I_{pulse} = −25 mA were alternately applied at H_x = +10 mT. After each M switching, the polarization-resolved spectra were recorded, and P_c was measured. To have a higher light intensity with a shorter acquisition time for electroluminescence spectra, we used a higher V_{bias} = 3.5 V. The P_c evolution as a function of the number of switching cycles in Fig. 3d shows very robust switching between the two states at +15% and −19%. The deviation of P_c in each state is less than 1%. Several selected electroluminescence spectra after different numbers of repetitions are shown in Extended Data Fig. 6. To further verify if there is any damage to the ferromagnet–semiconductor Schottky interface because of the switching current in the lateral injector channel, we measured the I–V_{bias} curves of spin-LED before and after the repetition measurement. As shown in Extended Data Fig. 7, the two I–V_{bias} curves almost coincide, which indicates that the Schottky barrier height is robust and negligibly affected by the switching current in the channel, thus validating the appropriate approach for P_c modulation. This is a striking difference from the previously tried spin injectors, which have shown a strong degradation of the ferromagnet–semiconductor interface after pulse-current switching (Supplementary Note 2). In Fig. 3e, we compare the switching of P_c with I_{pulse} and current-induced M switching measured by R_{AHE}, whereas detailed electroluminescence spectra measured after different pulse-current switching are shown in Extended Data Fig. 8. As P_c and R_{AHE} show similar hysteresis loops, this further demonstrates the connection between the P_c modulation and the M switching. Between I_{pulse} of 10 mA and 20 mA, there is a partial M switching, resulting in intermediate P_c states. By controlling the fraction of M switching with I_{pulse} and t_{pulse}, we are able to obtain multi-state P_c, which could enable a multi-level modulation coding, even for P_c modulation-based optical communications.

Outlook

Although our approach to transfer angular momentum between photons, electrons and ferromagnets was demonstrated in spin-LEDs, this electrical control of the polarization of light at room temperature and zero magnetic field also provides a key breakthrough to enable electrically injected spin-lasers. With its ultrathin metallic layers (<7 nm), our spin injector could be embedded directly in the optical cavity of a spin-laser. By placing the injector in a node of the stationary electromagnetic field beneath a dielectric-distributed Bragg reflector top mirror and close to the semiconductor-based optical gain region (Supplementary Note 7), the already low absorption and small magnetic circular dichroism of the magnetic layers can be further minimized while keeping a desirably short path for injected spins to the gain region. (Low optical absorption of typically 10% was demonstrated for a 5-nm layer thickness at 1-µm transmission wavelength[45], as well as a small magnetic circular dichroism of less than 1% (ref. 5), which can both further be reduced by an appropriate cavity design.) As our SOT-based spin-injection concept can be operated in a continuous-wave mode with a constant carrier density in the gain region under M switching (Supplementary Note 8), this enables to decouple modulating P_c from modulating the light intensity, crucial for future high-speed and secure data transmission. Independent advances in the fast M switching for magnetic memories could further enhance our implementation of SOT spin-LEDs and spin-lasers and stimulate the investigations into the ultimate speed limitations, perhaps reaching ps scale[30]. By reducing the mesa diameter from Fig. 1b

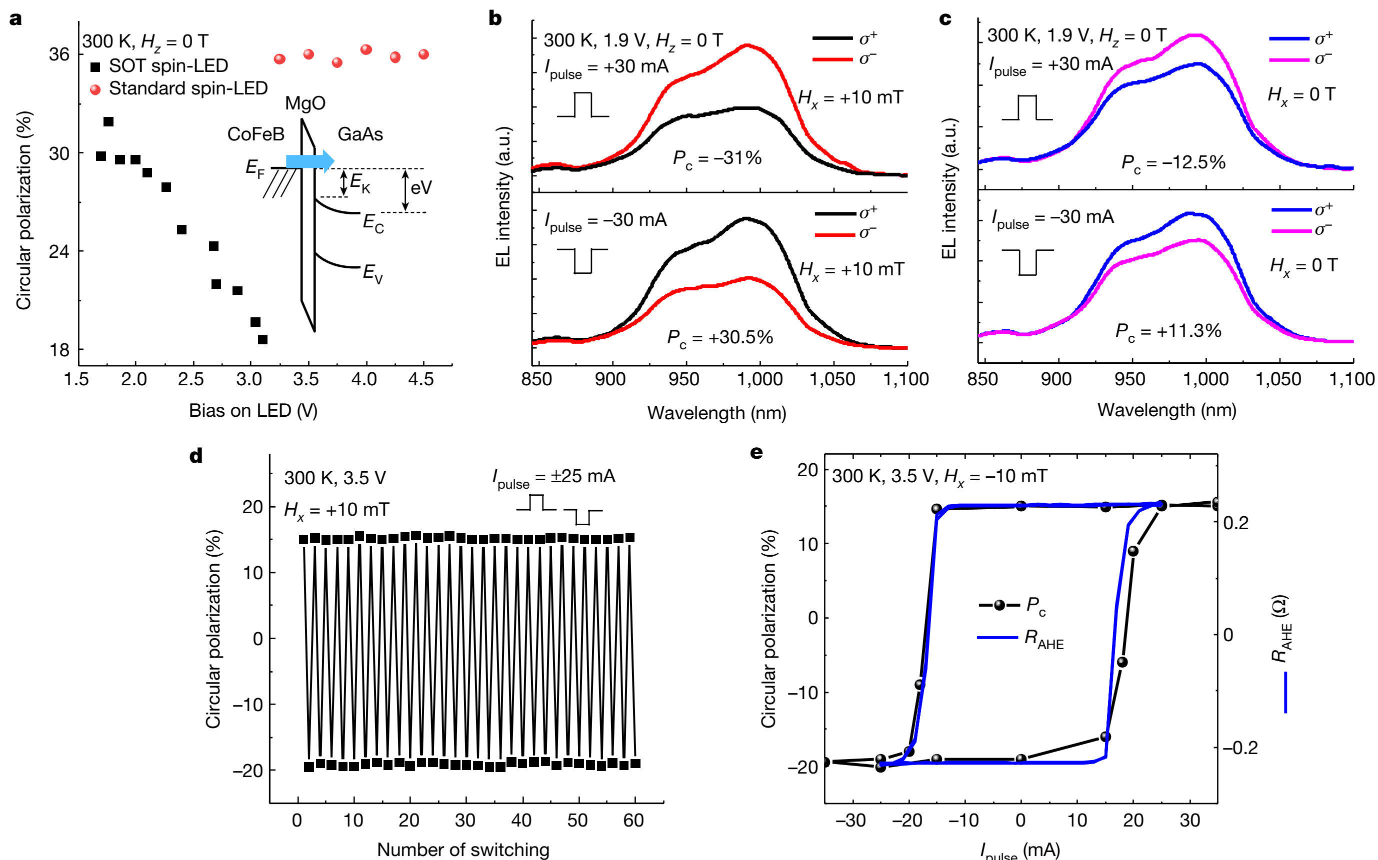

Fig. 3 | Polarization-resolved electroluminescence characterization and electrical control of circular polarization of spin-LEDs. a, Bias-dependent circular polarization at 300 K and H_z = 0 T for an SOT (black) and standard (red) spin-LED. Inset, schematic spin injection from the Fermi level, E_F, of the metal to the GaAs conduction band by tunnelling through the MgO barrier. With the applied bias, the electrons have a kinetic energy, E_k, injected into the GaAs layer. **b**,**c**, Electroluminescence spectra of SOT spin-LED measured at 300 K, V_{bias} = 1.9 V and H_z = 0 T, after one single pulse of magnetization switching. All spectra data have been smoothed by the 10-point FFT filter method. **b**, Switching with H_x = +10 mT and ±30 mA; **c**, Switching with H_x = 0 T and ±30 mA. **d**, Repetition measurement of P_c at 300 K and H_z = 0 with 30 cycles of magnetization switching. In each cycle, the magnetization is switched by two I_{pulse} for positive and negative 25 mA with H_x = +10 mT. **e**, Comparison of P_c and R_{AHE} loops as a function of I_{pulse}. Error bars are smaller than data points in **a**–**e**. a.u., arbitrary units; EL, electroluminescence.

to several µm, our concept enables realizing disruptive devices, including spin-controlled single-photon sources for optical quantum applications. With the spin–photon polarization conversion, this source produces high-yield circularly polarized single photons, increasing the probability of obtaining N indistinguishable photons by a factor of 2^N, compared with the unpolarized counterparts. This exponential increase will accelerate the development of quantum technologies. GHz polarization modulation of single photons would greatly increase the data bandwidth for quantum cryptographic communication, compared with Kbps–Mbps in the current quantum key distribution technology[46]. We also predict a scaled-down realization of our proposal relying on the growing family of two-dimensional ferromagnets and semiconductors with excellent optical and SOT properties[47,48]. As spin injection is not only an element of spintronic devices but also a sensitive spectroscopic tool to study various fundamental phenomena, such as the pairing symmetry of unconventional superconductors, skyrmion excitations in the quantum Hall regime, and spin-charge separation in non-Fermi liquids[2], our progress provides interesting prospects for spin-dependent time-resolved spectroscopies. Our scale-downed SOT-based spin injector and mesa would enable ultrafast electrical control of both spin injection and circular polarization of the emitted light, which could be used as a time-resolved, spin-resolved and spatially resolved probe in the optically or electrically detected spectroscopies, all at room temperature and in the absence of an applied magnetic field.

Online content

Any methods, additional references, Nature Portfolio reporting summaries, source data, extended data, supplementary information, acknowledgements, peer review information; details of author contributions and competing interests; and statements of data and code availability are available at https://doi.org/10.1038/s41586-024-07125-5.

1. Waser, R. (ed.) *Nanoelectronics and Information Technology: Advanced Electronic Materials and Novel Devices* 3rd edn (Wiley-VCH, 2012).
2. Žutić, I., Fabian, J. & Das Sarma, S. Spintronics: fundamentals and applications. *Rev. Mod. Phys.* **76**, 323–410 (2004).
3. Fiederling, R. et al. Injection and detection of a spin-polarized current in a light-emitting diode. *Nature* **402**, 787–790 (1999).
4. Giba, A. E. et al. Spin injection and relaxation in *p*-doped (In,Ga)As/GaAs quantum-dot spin light-emitting diodes at zero magnetic field. *Phys. Rev. Appl.* **14**, 034017 (2020).
5. Liang, S. H. et al. Large and robust electrical spin injection into GaAs at zero magnetic field using an ultrathin CoFeB/MgO injector. *Phys. Rev. B* **90**, 085310 (2014).
6. Gerhardt, N. C. et al. Electron spin injection into GaAs from ferromagnetic contacts in remanence. *Appl. Phys. Lett.* **87**, 032502 (2005).
7. Kim, Y.-H. et al. Chiral-induced spin selectivity enables a room-temperature spin light-emitting diode. *Science* **371**, 1129–1133 (2021).
8. Chernyshov, A. et al. Evidence for reversible control of magnetization in a ferromagnetic material by means of spin–orbit magnetic field. *Nat. Phys.* **5**, 656–659 (2009).
9. Miron, I. M. et al. Perpendicular switching of a single ferromagnetic layer induced by in-plane current injection. *Nature* **476**, 189–193 (2011).
10. Liu, L. et al. Spin-torque switching with the giant spin Hall effect of tantalum. *Science* **336**, 555–558 (2012).
11. Mishra, R., Kim, T., Park, J. & Yang, H. Shared-write-channel-based device for high-density spin-orbit-torque magnetic random-access memory. *Phys. Rev. Appl.* **15**, 024063 (2021).

12. Lindemann, M. et al. Ultrafast spin-lasers. *Nature* **568**, 212–215 (2019).
13. Miller, D. A. B. Attojoule optoelectronics for low-energy information processing and communications. *J. Lightwave Technol.* **35**, 346–396 (2017).
14. Sandvine. *The Global Internet Phenomena Report: COVID-19 Spotlight* https://go.nature.com/49HrzWl (2020).
15. Jones, N. How to stop data centres from gobbling up the world's electricity. *Nature* **561**, 163–166 (2018).
16. Dery, H. et al. Spintronic nanoelectronics based on magneto-logic gates. *IEEE Trans. Electron. Dev.* **59**, 259–262 (2012).
17. Vagionas, C. et al. Optical memory architectures for fast routing address look-up (AL) table operation. *J. Phys. Photon.* **1**, 044005 (2019).
18. Sherson, J. F. et al. Quantum teleportation between light and matter. *Nature* **443**, 557–560 (2006).
19. Zhan, X. et al. 3D laser displays based on circularly polarized lasing from cholesteric liquid crystal arrays. *Adv. Mater.* **33**, 202104418 (2021).
20. Nishizawa, N. & Munekata, H. Lateral-type spin-photonics devices: development and applications. *Micromachines* **12**, 644–675 (2021).
21. Ren, J.-G. et al. Ground-to-satellite quantum teleportation. *Nature* **549**, 70–73 (2017).
22. Žutić, I. et al. Spin-lasers: spintronics beyond magnetoresistance. *Solid State Commun.* **316–317**, 113949 (2020).
23. Zhang, Y. J., Oka, T., Suzuki, R., Ye, J. T. & Iwasa, I. Electrically switchable chiral light-emitting transistor. *Science* **344**, 725–728 (2014).
24. Marin, J. F. G. et al. Room-temperature electrical control of polarization and emission angle in a cavity-integrated 2D pulsed LED. *Nat. Commun.* **13**, 4884 (2022).
25. Nishizawa, N., Nishibayashi, K. & Munekata, H. A spin light emitting diode incorporating ability of electrical helicity switching. *Appl. Phys. Lett.* **104**, 111102 (2014).
26. Yokota, N., Nisaka, K., Yasaka, H. & Ikeda, K. Spin polarization modulation for high-speed vertical-cavity surface-emitting lasers. *Appl. Phys. Lett.* **113**, 171102 (2018).
27. Sinova, J. & Žutić, I. New moves of the spintronics tango. *Nat. Mater.* **11**, 368–371 (2012).
28. Holub, M., Shin, J., Saha, D. & Bhattacharya, P. Electrical spin injection and threshold reduction in a semiconductor laser. *Phys. Rev. Lett.* **98**, 146603 (2007).
29. Tsymbal, E. Y. & Žutić, I. *Spintronics Handbook: Spin Transport and Magnetism* 2nd edn (CRC Press, Boca Raton, FL, 2019).
30. Jhuria, K. et al. Spin–orbit torque switching of a ferromagnet with picosecond electrical pulses. *Nat. Electron.* **3**, 680–686 (2020).
31. Li, H. et al. Field-free deterministic magnetization switching with ultralow current density in epitaxial Au/Fe_4N bilayer films. *ACS Appl. Mater. Interfaces* **11**, 16965–16971 (2019).
32. van den Brink, A. Field-free magnetization reversal by spin-Hall effect and exchange bias. *Nat. Commun.* **7**, 10854 (2016).
33. Liu, L. et al. Symmetry-dependent field-free switching of perpendicular magnetization. *Nat. Nanotechnol.* **16**, 277–282 (2021).
34. Pelucchi, E. et al. The potential and global outlook of integrated photonics for quantum technologies. *Nat. Rev. Phys.* **4**, 194–208 (2022).
35. Fang, C. et al. Observation of the fluctuation spin Hall effect in a low-resistivity antiferromagnet. *Nano Lett.* **23**, 11485–11492 (2023).
36. Lee, S. et al. Efficient conversion of orbital Hall current to spin current for spin-orbit torque switching. *Commun. Phys.* **4**, 234 (2021).
37. Xie, H. et al. Orbital torque of Cr-induced magnetization switching in perpendicularly magnetized Pt/Co/Pt/Cr heterostructures. *Chin. Phys.* **32**, 037502 (2023).
38. Kumar, S. & Kumar, S. Ultrafast THz probing of nonlocal orbital current in transverse multilayer metallic heterostructures. *Nat. Commun.* **14**, 8185 (2023).
39. Zhang, C. et al. Magnetotransport measurements of current induced effective fields in Ta/CoFeB/MgO. *Appl. Phys. Lett.* **103**, 262407 (2013).
40. Yu, G. et al. Switching of perpendicular magnetization by spin–orbit torques in the absence of external magnetic fields. *Nat. Nanotechnol.* **9**, 548–554 (2014).
41. Rahaman, S. Z. et al. Pulse-width and temperature effect on the switching behavior of an etch-stop-on-MgO-barrier spin-orbit torque MRAM cell. *IEEE Electron Device Lett.* **39**, 1306–1309 (2018).
42. Zhang, X., Vernier, N., Zhao, W., Vila, L. & Ravelosona, D. Extrinsic pinning of magnetic domain walls in CoFeB-MgO nanowires with perpendicular anisotropy. *AIP Adv.* **8**, 056307 (2018).
43. Barate, P. et al. Bias dependence of the electrical spin injection into GaAs from Co–Fe–B/MgO injectors with different MgO growth processes. *Phys. Rev. Appl.* **8**, 054027 (2017).
44. Iba, S., Koh, S., Ikeda, K. & Kawaguchi, H. Room temperature circularly polarized lasing in an optically spin injected vertical-cavity surface-emitting laser with (110) GaAs quantum wells. *Appl. Phys. Lett.* **98**, 081113 (2011).
45. Frougier, J. et al. Control of light polarization using optically spin-injected vertical external cavity surface emitting lasers. *Appl. Phys. Lett.* **103**, 252402 (2013).
46. Diamanti, E., Lo, H.-K., Qi, B. & Yuan, Z. Practical challenges in quantum key distribution. *npj Quantum Inf.* **2**, 16025 (2016).
47. Žutić, I., Matos-Abiague, A., Scharf, B., Dery, H. & Belashchenko, K. Proximitized materials. *Mater. Today* **22**, 85–107 (2019).
48. Sierra, J. F., Fabian, J., Kawakami, R. K., Roche, S. & Valenzuela, S. O. Van der Waals heterostructures for spintronics and opto-spintronics. *Nat. Nanotechnol.* **16**, 856–868 (2021).

Publisher's note Springer Nature remains neutral with regard to jurisdictional claims in published maps and institutional affiliations.

Springer Nature or its licensor (e.g. a society or other partner) holds exclusive rights to this article under a publishing agreement with the author(s) or other rightsholder(s); author self-archiving of the accepted manuscript version of this article is solely governed by the terms of such publishing agreement and applicable law.

© The Author(s), under exclusive licence to Springer Nature Limited 2024, corrected publication 2024

Methods

Sample preparation

The spin-LED structure contains two parts: the semiconductor LED and the metallic spin injector. The *p*-*i*-*n* LED device was grown by molecular beam epitaxy (MBE) containing a single layer of InAs quantum dots embedded in the active region. The full structure is as follows: *p*+-GaAs:Zn (001) substrate ($p = 3 \times 10^{18}$ cm^{-3})/300 nm *p*-GaAs:Be ($p = 2 \times 10^{18}$ cm^{-3})/400 nm *p*-$Al_{0.3}Ga_{0.7}As$:Be ($p = 2 \times 10^{18}$–5×10^{17} cm^{-3})/30 nm *i*-GaAs with Be δ-doping in the centre/InAs quantum dot/30 nm *i*-GaAs/50 nm *n*-GaAs:Si ($n = 1 \times 10^{16}$ cm^{-3}). The role of the Be δ-doping is to form *p*-doped InGaAs quantum dots. This growth method allows to precisely control the doping concentration in the quantum dots, which is optimized to an average of one dopant per quantum dot. The reason for the need for *p*-doped quantum dots is the following. The eigenstates of neutral quantum dots are linearly polarized because of the anisotropic electron–hole exchange interaction, resulting in only a vanishing or weak circular polarization of the emitted light[49]. By contrast, in *p*-doped quantum dots, the exchange interactions between the electron and the two holes within the positively charged exciton cancel each other[50], resulting in circularly polarized eigenstates (even in the absence of an external magnetic field), which leads to large circular polarization of the light and long electron spin-relaxation time, both desirable for the operation of our spin-LEDs. Supplementary Note 3 provides more structural and chemical characterizations of InAs quantum dots.

The LED was passivated with arsenic in an MBE chamber and transferred by air to a second inter-connected MBE-sputtering system in which the As capping layer was desorbed at 300 °C. Next, the sample was transferred to a sputtering chamber under an ultrahigh vacuum to grow the spin injector. The structure of the spin injector is MgO(2.5 nm)/$Co_{0.4}Fe_{0.4}B_{0.2}$(1.2 nm)/Ta(3 nm). Afterwards, the sample was transferred back to the MBE and a 3-nm thick Cr layer was deposited on the top. Two types of spin-LEDs were processed with UV photolithography and etching techniques. One is a standard spin-LED device with a circular mesa and spin injector of a diameter of 500 µm. The other is a SOT spin-LED with a spin injector in a Hall bar shape, as shown in Fig. 1b. The channel length and width are 50 µm and 20 µm, respectively. Finally, the processed wafers were cut into small pieces to perform rapid temperature annealing at 300 °C for 3 min to establish the PMA of the spin injector. More details concerning the growth and the optimization of the PMA spin injector can be found in refs. 4,5,51,52.

Structural and chemical characterization of spin injectors

The interface of the spin injector was investigated by HR-STEM combined with spatially resolved electron energy loss spectroscopy (EELS). These characterizations were performed using a probe-corrected microscope JEOL ARM200F equipped with a GATAN GIF quantum energy filter to reveal the structure and element distribution. The microscope was operated at 200 kV. The EELS spectrum images were recorded with a probe current of about 50 pA. The two EELS spectrum images were simultaneously recorded: one for the low-loss part containing zero loss and the other for the core loss, which allows advanced data post-processing. Thin lamellas were prepared by focused ion beam (FIB) milling using an FEI Helios Nanolab 600i dual beam.

Extended Data Fig. 1a shows a low-magnification STEM high-angle annular dark-field (HAADF) image showing the quantum-dot-based spin-LED structure. The quantum-dot layer appears as a light-grey line in the middle of the micrograph. The spin injector exhibits a very good homogeneity on the top of the LED. Extended Data Fig. 1b shows the magnified HR-STEM bright-field image of the injector structure. Here the contrasts are inverted as compared with the HAADF image and the interferential contrast is visible in the crystalline parts. The MgO layer exhibits a clear (001) texture with an abrupt interface between the GaAs and CoFeB layers. Although the Ta/CoFeB interface appears rather diffuse, we can still confirm the continuity of the 1.2-nm thick CoFeB layer. After annealing at 300 °C, the CoFeB layer is crystallized. On the right, the fast Fourier transform (FFT) in different layers shows good crystallinity and epitaxial features between GaAs [110] (001)// MgO [110] (001)//CoFe [100] (001) (ref. 51).

Extended Data Fig. 1c shows quantitative chemical maps generated by processing the EELS spectrum images. The clear-layered structures of Ga, As, O, Fe and Co elements prove that no evident interdiffusion occurs from the ferromagnet layer to the MgO and GaAs layers, thus demonstrating that MgO acts as an efficient diffusion barrier. Moreover, the B atoms are found to strongly diffuse into the Ta layer after annealing at 300 °C, which is important for establishing the PMA at the MgO/CoFeB interface[5,51]. To qualitatively identify the interfacial diffusion, semi-quantitative profiles of the normalized content of each element are plotted in Extended Data Fig. 1d. Each point in the profile is extracted by integrating the elemental signals of the EELS maps from an area of 0.2 nm in height (about 1 atomic column) and 10 nm in width, parallel to the interfaces. The chemical distribution profiles show that B diffuses into Ta because of the crystallization of CoFeB from the MgO side[53]. A perfect overlap of Co and Fe is found, in contrast to the previous samples in which the MgO/CoFeB interface was Fe enriched[51]. We also find a slight oxidation of CoFe at the MgO interface for about one to two planes of thickness (as a small shift between Mg and O signals). A small diffusion of Ta into the CoFe layer and a small interdiffusion between Ta and Cr at the Ta/Cr interface can also be detected. As for the Cr capping layer, a part of it is oxidized. A small oxygen content detected elsewhere in Cr and Ta comes from the surface oxidation of the TEM lamella during the air exposure at the time of the transfer between the FIB milling system, vacuum storage and TEM. The high background for Ga is because of a small Ga implantation in the TEM lamella due to the FIB milling procedure.

Polarization-resolved electroluminescence characterization of standard and SOT spin-LEDs

For the polarization-resolved electroluminescence measurements, the electroluminescence signal is detected in a Faraday geometry and analysed by a spectrometer (Acton SP2500 Princeton Instruments) equipped with an 80 grooves per mm grating (blazed at 870 nm) and detected by an Si-based CCD camera (Pylon Excelon 400 BR from Princeton Instruments). The P_c of the electroluminescence is analysed by a quarter-wave retarder and a linear polarizer. All spectra data have been smoothed by 10-point FFT filter method. As the wavelength of the light emitted by the spin-LED approaches the limitation of the Si-based detector, the shape of the EL spectra is partially deformed, resulting in a change of the peak position of about 20 nm at room temperature (Supplementary Note 5). However, the wavelength dependence of P_c shows only a very slight difference around the electroluminescence peak wavelength (about 1%), for which the P_c value is analysed in this work.

Extended Data Fig. 3a (insets) shows the typical polarization-resolved electroluminescence spectra measured from a SOT spin-LED at 300 K and $V_{bias} = 3.5$ V with a current density of 8.2 A cm^{-2} at $H_z = 0$ T. In these spectra, we can observe a two-peak feature, one is centred at about 1 µm corresponding mainly to the emission of the X^+ trion transition (one electron and two holes forming a spin singlet) from the quantum-dot ensemble. The other peak, located at 930 nm, corresponds to the emission from the InGaAs wetting layer. This peak becomes less important in the net spectra after taking into account the total response efficiency of the spectrometer and CCD camera (Supplementary Note 5). The left and right insets correspond to the measurements in which the sample *M* is first saturated with a positive and negative 15 mT field, respectively. In both cases, we measured a large difference in the electroluminescence intensities for the right ($S^{\sigma+}$) and left ($S^{\sigma-}$) circularly polarized components at zero field. The electroluminescence P_c can be determined to be about +15.5% and −18.5% in the left and right insets, respectively. Although a spurious component due to magnetic circular

dichroism could artificially increase the measured P_c, it is estimated to be less than 1% for such a thin CoFeB layer (1.2 nm) (ref. 5). As shown in Extended Data Fig. 3a, the behaviour of P_c shows a clear hysteresis loop as a function of an applied magnetic field, which matches well the hysteresis loop in M, measured from an unpatterned sample by a superconducting quantum interference device at room temperature. This provides strong support that the large remnant P_c observed at $H_z = 0$ T is because of the injection of spin-polarized charge carriers from the ultrathin CoFeB layer with PMA. The sign change of the P_c is because of the M reversal of the spin injector. Slightly different P_c amplitudes for the two saturation states are probably because of a partial non-reversible magnetic domain pinned at the CoFeB/MgO interface.

We also investigated the temperature, T, dependence of P_c for the standard spin-LED (Extended Data Fig. 3b). It is interesting to find that the P_c increases with T and saturates for $T > 250$ K. Detailed electroluminescence spectra measured at different T are shown in Extended Data Fig. 5. It is found that the intensity of the peak assigned to the InGaAs wetting layer (shorter wavelength side) increases with T, indicating that a fraction of the electrons injected into the quantum dot have escaped and recombined in the wetting layer at high T. It is convenient to relate P_c and the spin polarization of the injected electrons, P_e, using $P_c = F \cdot P_e$, with the renormalization factor $F = 1/(1 + \tau/\tau_s)$ (refs. 2,54), which describes the reduction of the injected spin polarization at the time of carrier recombination, where τ and τ_s are the carrier and spin lifetimes of the electrons in the quantum dot, respectively. In III–V semiconductors, the reduction of the injected spin polarization is dominated by the DP spin-relaxation mechanism[2]. It is well known that CoFeB has a high Curie temperature (>750 K) (ref. 55), leading to the nearly constant P_e for T between 10 K and 300 K. Therefore, $P_c(T)$ should reflect the change of the F factor inherent to the semiconductor part rather than to the spin injector. To extract τ and τ_s, we have performed time-resolved photoluminescence (TRPL) measurements on an identical quantum-dot LED substrate (see details below). As shown in Extended Data Fig. 3c, both τ and τ_s decrease with T. However, the drop of τ is much larger than that of τ_s, resulting in an increase of F from 0.2 at 100 K to 0.53 at 300 K. The evolution of F follows well the same trend as the variation of P_c, thus explaining that the increase of P_c at room temperature is mainly because of the reduction of the carrier lifetime in the quantum dot. With the extracted F factor of 0.53 and P_c of 35% at room temperature, we can deduce the injected spin polarization P_e of about 66%, which is close to the spin polarization of bulk CoFeB ($P_0 = 65\%$) measured by point-contact Andreev reflection[56]. Two opposite effects are relevant for our spin-LEDs: (1) spin relaxation and depolarization during the transport across the GaAs layer, before the electron–hole recombination[2,4], which reduces the injected spin polarization and (2) MgO spin filtering, which enhances the injected spin polarization beyond what would be expected from the ferromagnet for CoFeB (refs. 29,57). Therefore, the figure of merit of spin injection (P_e/P_0) in our spin-LED is close to 100%. The spin-filtering mechanism in the MgO is well known. Its band structure enables electrons with orbital symmetry Δ_1 to pass through the barrier with the smallest decay compared with electrons with other orbital symmetries of an evanescent wavefunction inside the barrier[29,58–60,61]. In this case, MgO can effectively enhance the spin polarization for spin injection because Δ_1 electrons in the Fe band structure have the highest spin polarization at the Fermi level (half-metallic property with about 100% spin polarization).

The high P_c measured at zero magnetic field in the quantum-dot spin-LED at room temperature is almost four times larger than our previously reported P_c values (8%) in the QW-based spin-LED with the same type of PMA spin injector[5]. The reason why our previous quantum-dot spin-LEDs[4] cannot operate at room temperature is mainly because of the lower In concentration in the quantum dots. The higher In concentration in this work results in a smaller bandgap and better confinement of electrons and holes at high T. Furthermore, owing to the smaller τ at room temperature, we can obtain a twice larger P_c than previously reported in quantum-dot-based spin-LEDs (19%) (ref. 4). The high P_c value also exceeds the highest room temperature record (32%) reported with in-plane magnetized spin injectors[62] in the same detection geometry (Faraday geometry, see the benchmark of spin-LED work in Supplementary Note 6). In that case, a large applied magnetic field up to 5 T was required to orient M to the out-of-plane direction (recall also a similar situation in Supplementary Fig. S1b).

Time-resolved photoluminescence and the extraction of spin and carrier lifetimes

Short laser pulses from a mode-locked Ti:sapphire laser with a 2 ps pulse width were used for non-resonant circularly polarized excitation at a centre wavelength of 810 nm (1.531 eV). The TRPL signal was analysed with a temporal (spectral) resolution of 2.7 ps (5 nm) using a streak camera (Hamamatsu C5680, S-1 cathode) in combination with a spectrometer (Bruker Chromex 250IS). To analyse P_c, the TRPL signal was detected through a quarter-wave retarder and a linear polarizer.

Extended Data Fig. 9a shows the TRPL intensity as a function of photon wavelength at 100 K. Two peaks can be found, one is related to the GaAs barrier and the other is related to the quantum-dot layer. To extract the carrier and spin lifetimes, τ and τ_s, we focus on the quantum-dot spectrum. As an example, we show in the Extended Data Fig. 9b TRPL intensity evolution for the $S^{\sigma+}$ and $S^{\sigma-}$ components measured at 300 K. τ can be extracted from the exponential fit of the photoluminescence curve ($S^{\sigma+} + S^{\sigma-}$) to be about 37.8 ps (Extended Data Fig. 9c). To extract τ_s, we have studied the P_c dynamics, recalling that $P_c = (S^{\sigma+} - S^{\sigma-})/(S^{\sigma+} + S^{\sigma-})$. Extended Data Fig. 9d shows P_c as a function of time. The decay time of P_c that corresponds to τ_s can be extracted from the exponential fit to be 43.3 ps at 300 K.

Data availability

All data generated and analysed in this work are available in a Zenodo repository (https://zenodo.org/records/10666881).

49. Belhadj, T. et al. Controlling the polarization eigenstate of a quantum dot exciton with light. *Phys. Rev. Lett.* **103**, 086601 (2009).
50. Braun, P. F. et al. Direct observation of the electron spin relaxation induced by nuclei in quantum dots. *Phys. Rev. Lett.* **94**, 116601 (2005).
51. Tao, B. et al. Atomic-scale understanding of high thermal stability of the Mo/CoFeB/MgO spin injector for spin-injection in remanence. *Nanoscale* **10**, 10213–10220 (2018).
52. Cadiz, F. et al. Electrical initialization of electron and nuclear spins in a single quantum dot at zero magnetic field. *Nano Lett.* **18**, 2381–2386 (2018).
53. Lu, Y. et al. Depth analysis of boron diffusion in MgO/CoFeB bilayer by X-ray photoelectron spectroscopy. *J. Appl. Phys.* **108**, 043703 (2010).
54. Liu, B. et al. Spin injection probed by combined optical and electrical techniques in spin-LED. *Phys. Status. Solidi. (c)* **1**, 475–478 (2004).
55. Lee, K.-M., Choi, J. W., Sok, J. & Min, B.-C. Temperature dependence of the interfacial magnetic anisotropy in W/CoFeB/MgO. *AIP Adv.* **7**, 065107 (2017).
56. Huang, S. X., Chen, T. Y. & Chien, C. L. Spin polarization of amorphous CoFeB determined by point-contact Andreev reflection. *Appl. Phys. Lett.* **92**, 242509 (2008).
57. Barate, P. et al. Electrical spin injection into InGaAs/GaAs quantum wells: A comparison between MgO tunnel barriers grown by sputtering and molecular beam epitaxy methods. *Appl. Phys. Lett.* **105**, 012404 (2014).
58. Butler, W. H., Zhang, X.-G., Schulthess, T. C. & MacLaren, J. M. Spin-dependent tunneling conductance of Fe|MgO|Fe sandwiches. *Phys. Rev. B* **63**, 054416 (2001).
59. Yuasa, S., Nagahama, T., Fukushima, A., Suzuki, Y. & Ando, K. Giant room-temperature magnetoresistance in single-crystal Fe/MgO/Fe magnetic tunnel junctions. *Nat. Mater.* **3**, 868–871 (2004).
60. Parkin, S. S. P. et al. Giant tunnelling magnetoresistance at room temperature with MgO (100) tunnel barriers. *Nat. Mater.* **3**, 862–867 (2004).
61. Lu, Y. et al. Spin-orbit coupling effect by minority interface resonance states in single-crystal magnetic tunnel junctions. *Phys. Rev. B* **86**, 184420 (2012).
62. Jiang, X. et al. Highly spin-polarized room-temperature tunnel injector for semiconductor spintronics using MgO(100). *Phys. Rev. Lett.* **94**, 056601 (2005).

Acknowledgements We acknowledge B. Tao, S. Liang, A. Djeffal, T. H. Pham, J.-Y. Chen and M. Hehn for their contribution to the previous development of spin injectors. We thank S. Suire and C. Robert for their assistance with electroluminescence setups and L. Pasquier, O. Lerbert and D. Pierre for their help with MBE maintenance. We also acknowledge D. Crete for the discussion of the shunting problem. We appreciate the discussions on SOT spin-LEDs with A. Fert and Z.-G. Wang. We thank M. Hofmann for his support with the time-resolved photoluminescence measurements. This work is supported by the French National Research

Agency (ANR) SOTspinLED project (no. ANR-22-CE24-0006-01), by the German Research Foundation (DFG) within the Reinhart-Koselleck-Project (no. 490699635), by the US National Science Foundation (NSF) Electrical, Communications and Cyber Systems grant no. 2130845 (I.Ž. for LEDs) and by the US Department of Energy (DOE) Office of Science Basic Energy Sciences (BES) award no. DE-SC0004890 (I.Ž. for SOT). This work is also partially financially supported by the National Natural Science Foundation of China (NSFC, grant no. 12134017). J.-P.W. thanks the partial support from the Robert Hartmann Endowed Chair Professorship and the National Science Foundation SHF: Small: Collaborative Research: Energy efficient strain-assisted spin transfer torque memory. We thank the French RENATECH network for the support of semiconductor growth and partial support from 'Lorraine Université d'Excellence' project (no. ANR-15-IDEX-04-LUE). The experiments were performed using equipment from the CC-DAUM, CC-MINALOR, CC-3M and CC-MAGCRYO platforms funded by FEDER (EU), ANR, the Region Lorraine and the metropole of Grand Nancy.

Author contributions Y.L. coordinated the research project. Y.L., P.A.D., J.-M.G., H.J., A.L. and M.M. conceived the sample structure. P.A.D., A.B., P.P., M.V. and J.-P.W. contributed to the fabrication of the spin injector. M.M., B.X. and A.L. grew the LED structure. P.A.D., P.R., L.L., D.L., M.S., G.C. and H.R. contributed to the electroluminescence characterizations. M.L. and N.C.G. carried out the TRPL characterizations. P.A.D., N.F.P., T.C., T.M., J.-M.G., H.J. and J.-C.R.S. characterized the magnetization switching of the spin injector. N.F.P. and P.A.D. performed the Kerr microscopy measurements. X.D. and P.A.D. performed the TEM characterizations. Y.L., I.Ž. and N.C.G. prepared the paper, with the help of P.A.D., X.D., P.R., X.M., M.C.B., H.J., J.-P.W., S.M. and X.H. All authors analysed the data, discussed the results and commented on the paper.

Competing interests The authors declare no competing interests.

Additional information

Supplementary information The online version contains supplementary material available at https://doi.org/10.1038/s41586-024-07125-5.

Correspondence and requests for materials should be addressed to Yuan Lu.

Peer review information *Nature* thanks the anonymous reviewers for their contribution to the peer review of this work.

Reprints and permissions information is available at http://www.nature.com/reprints.

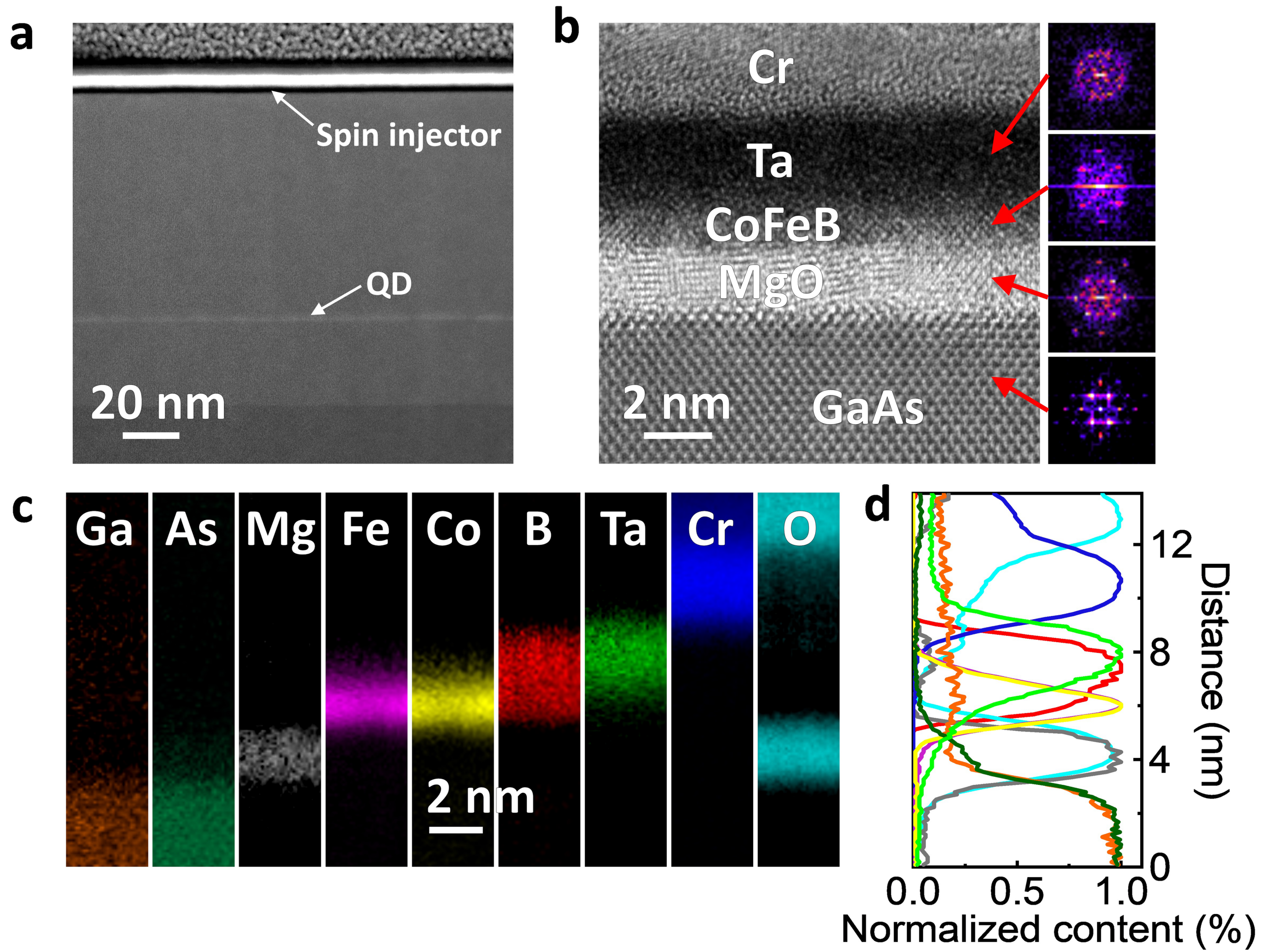

Extended Data Fig. 1 | Interfacial structure and chemical characterization of the spin injector. a, Large-scale HR-STEM HAADF image showing a good homogeneity of the QD spin-LED multilayer structure. **b**, Enlarged HR-STEM BF image showing the injector multilayer structure. **c**, Maps for individual elements drawn from processed EELS spectrum images. **d**, Elemental profiles extracted from the maps of elements. The colors of the profile lines are consistent with the colors of the elemental maps in **c**.

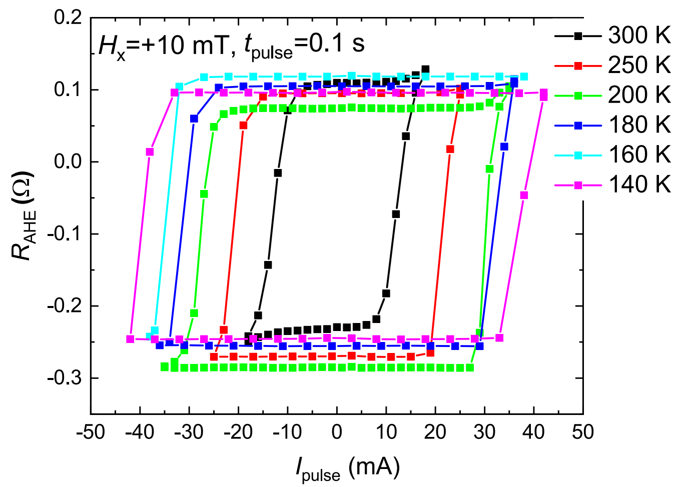

Extended Data Fig. 2 | R_{AHE} of spin injector with a reversal of the in-plane H_x (compared to Fig. 2b in the main text). R_{AHE} of spin injector as a function of pulsed current, I_{pulse}, with the duration of t_{pulse} = 0.1 s, at different temperatures with a small in-plane field H_x = +10 mT.

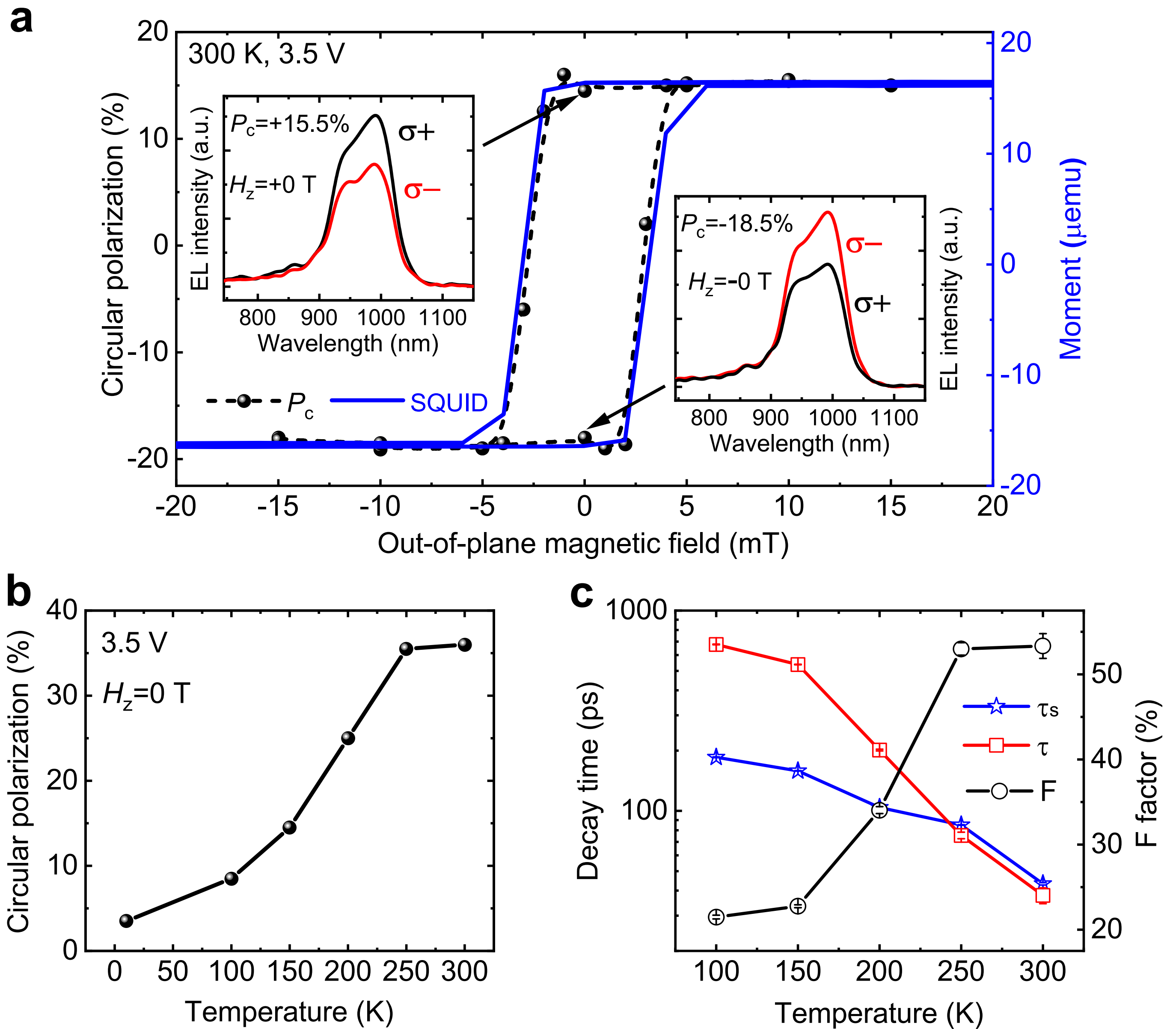

Extended Data Fig. 3 | Polarization-resolved electroluminescence characterization of spin-LEDs. **a**, P_c of the SOT spin-LED under bias, V_{bias} = +3.5 V (dashed lines with symbols) as a function of the out-of-plane magnetic field, H_z, and the corresponding SQUID hysteresis loop (blue solid line) measured at 300 K, respectively. The insets show the EL spectra measured at zero field, where H_z = ±0 T indicate that the sample M is first saturated by H_z = ±15 mT, respectively. **b**, $P_c(T)$ of a standard spin-LED at a fixed V_{bias} = 3.5 V and H_z = 0 T. **c**, T dependence of τ and τ_s measured from the TRPL characterization, while the T dependence of the F factor is deduced from $1/(1+\tau/\tau_s)$. The error bars shown in (**c**) result from the fits of the time transients (see Extended Data Fig. 9).

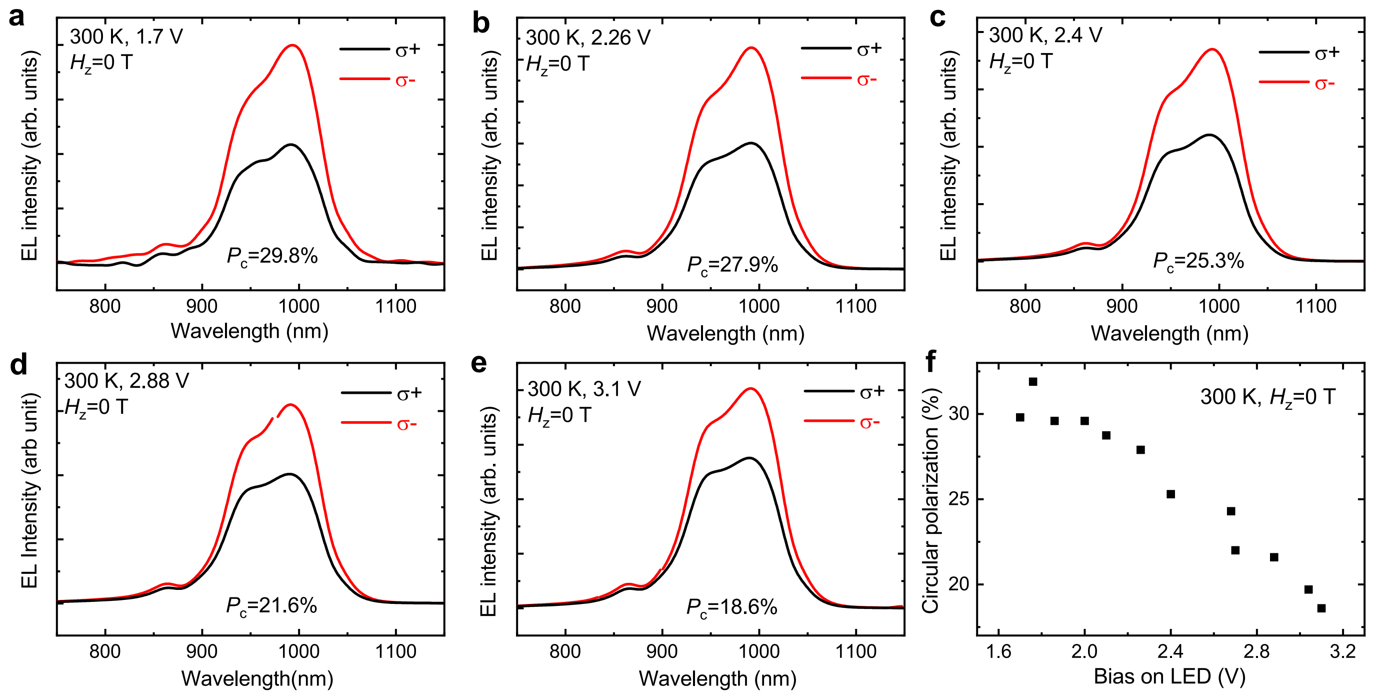

Extended Data Fig. 4 | Bias dependence of circular polarization measured in the SOT spin-LED. a–e, EL spectra of the SOT spin-LED measured at 300 K and H_z = 0 T, with V_{bias}: (**a**) 1.7 V, (**b**) 2.26 V, (**c**) 2.4 V, (**d**) 2.88 V, (**e**) 3.1 V. **f**, P_c as a function of V_{bias} at 300 K and H_z = 0 T, for the SOT spin-LED.

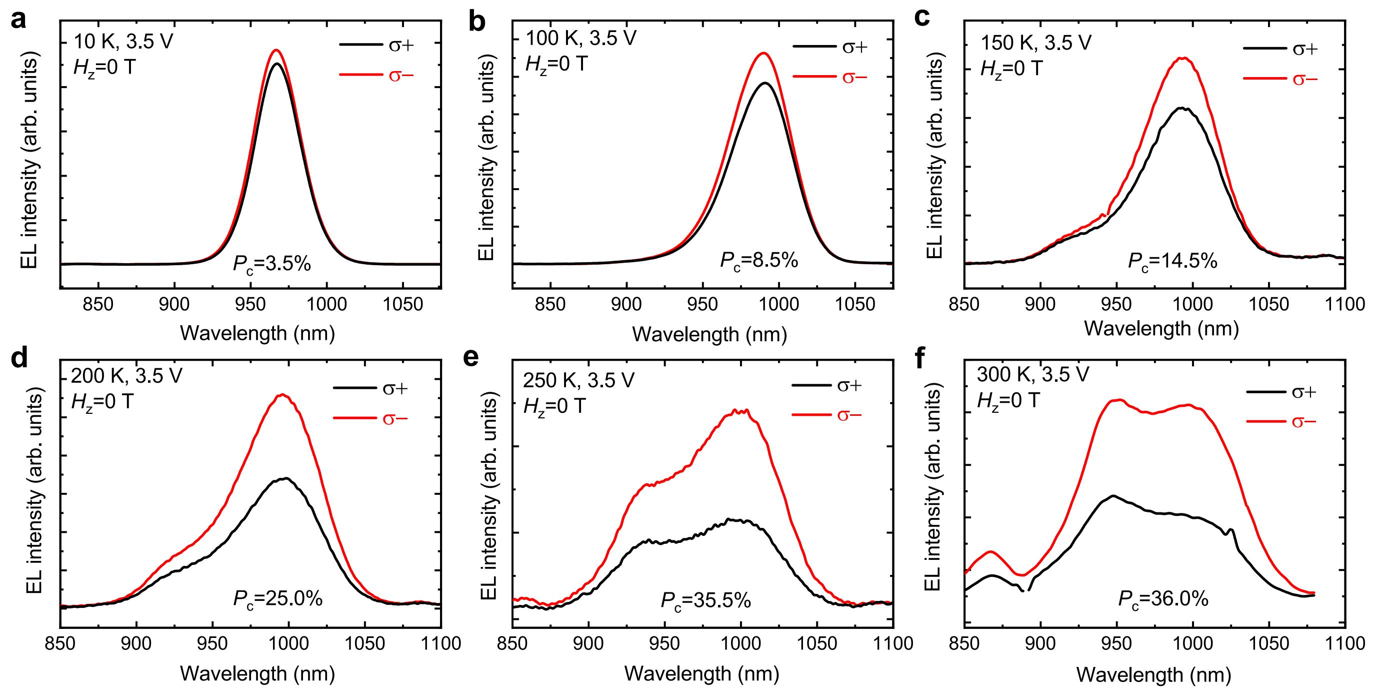

Extended Data Fig. 5 | Temperature dependence of circular polarization measured in the standard spin-LED. a–f, EL spectra of the standard spin-LED measured at H_z = 0 T, with V_{bias} = 3.5 V and different T. (**a**) 10 K, (**b**) 100 K, (**c**) 150 K, (**d**) 200 K, (**e**) 250 K, (**f**) 300 K.

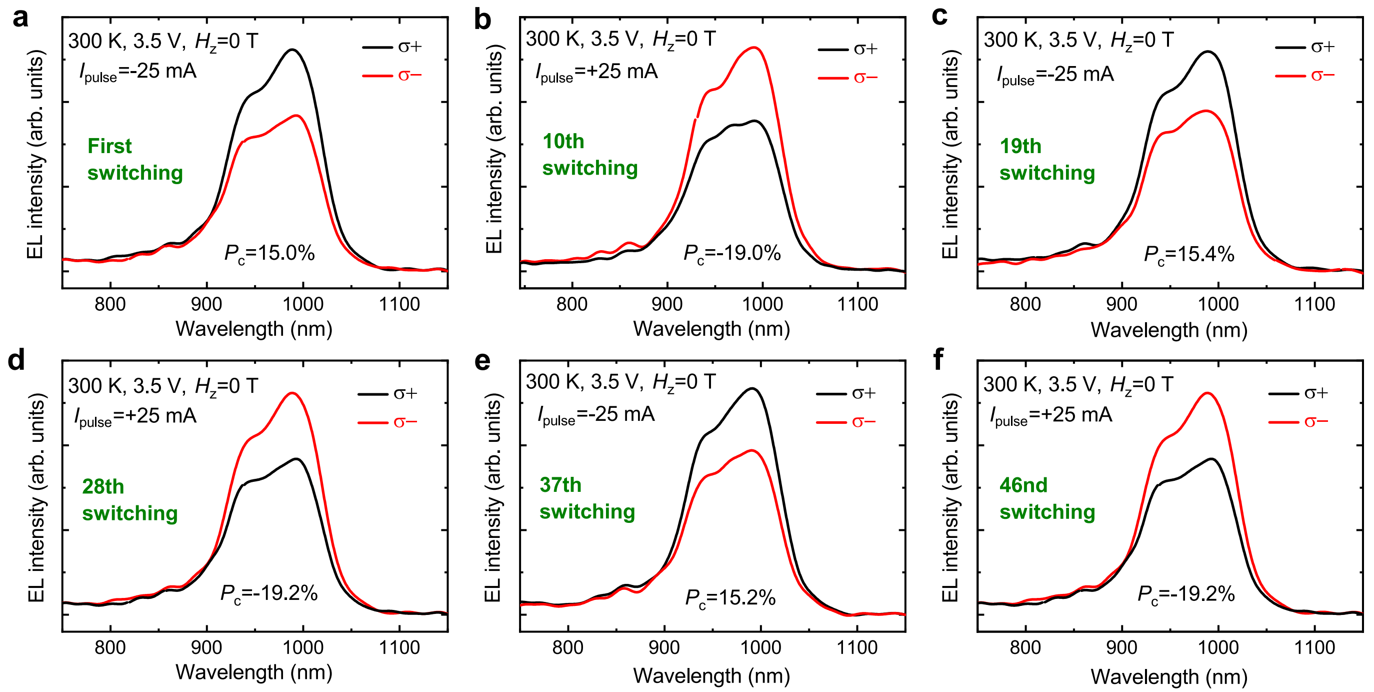

Extended Data Fig. 6 | Repetition measurement of P_c at 300 K after different number of switching. EL spectra of the SOT spin-LED measured at H_z = 0 T and V_{bias} = 3.5 V with a repetition of a single pulsed current *M* switching. **a**, First switching, **b**, 10th switching, **c**, 19th switching, **d**, 28th switching, **e**, 37th switching, and **f**, 46nd switching.

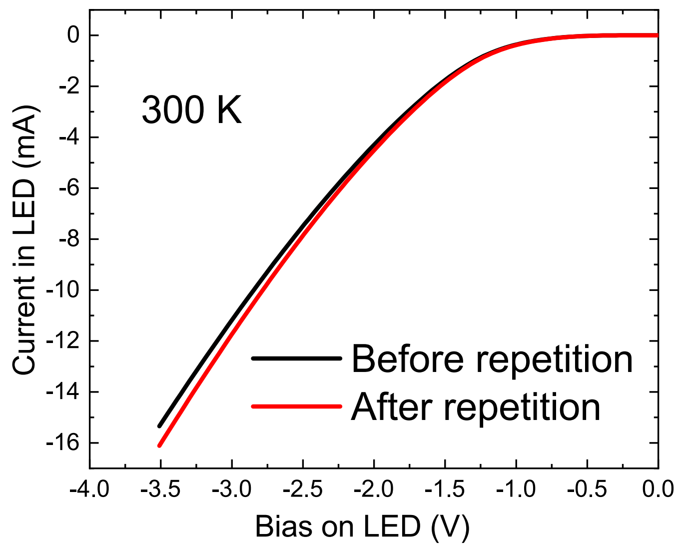

Extended Data Fig. 7 | Stability of the ferromagnet/semiconductor Schottky interface after magnetization switching. I–V_{bias} curves of the SOT spin-LED measured before and after the repetition switching at 300 K.

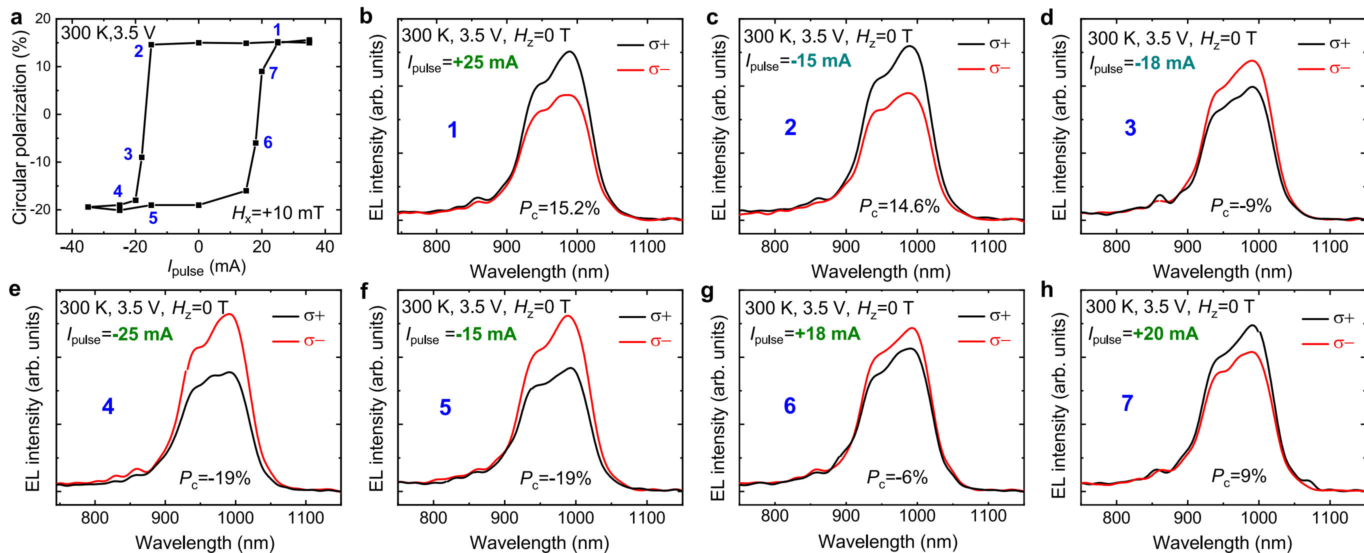

Extended Data Fig. 8 | P_c loop as a function of pulsed switching current. **a**, P_c loop as a function of the switching pulsed current, I_{pulse}, measured at 300 K. Each M switching is at H_x = +10 mT. **b**-**h**, EL spectra of the SOT spin-LED measured at H_z = 0 T and V_{bias} = 3.5 V after M switching corresponding to each point numbered in (**a**). For one loop, it starts from (**b**) +25 mA to (**c**) −15 mA, (**d**) −18 mA, (**e**) −25 mA, (**f**) −15 mA, (**g**) +18 mA, and (**h**) +20 mA.

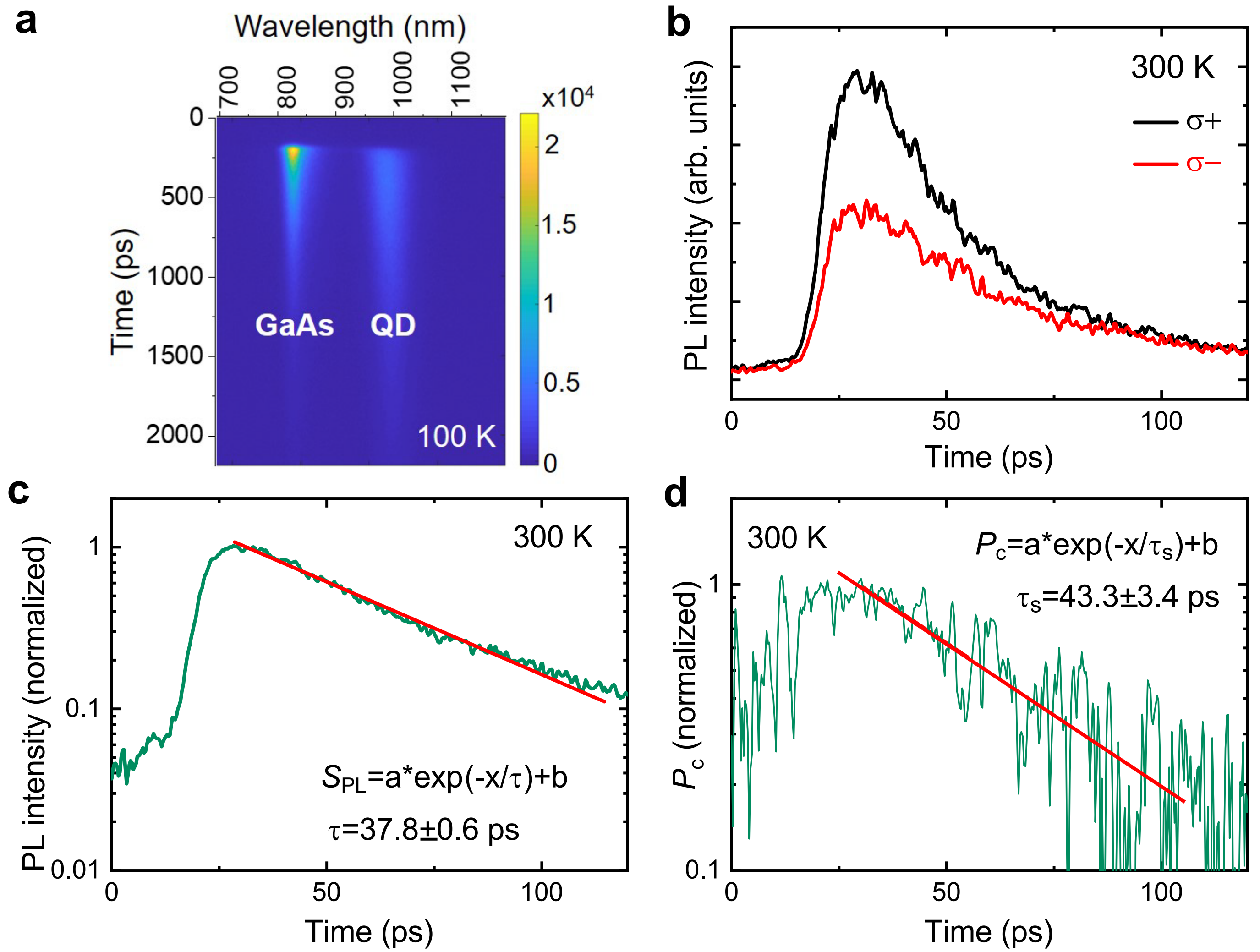

Extended Data Fig. 9 | Time-resolved photoluminescence and the extraction of spin and carrier lifetimes. a, Typical PL intensity mapping at 100 K for QD LEDs as a function of time and photon wavelength. **b**, QD TRPL intensity evolution for the $S^{\sigma+}$ and $S^{\sigma-}$ components measured at 300 K. **c**, Determination of τ from the exponential fit of the decay time for the PL intensity ($S^{\sigma+} + S^{\sigma-}$). **d**, Determination of τ_s from the exponential fit of the decay time of P_c. The error bars shown in (**c**,**d**) result from the fits of the time transients.